CrossMark

ORIGINAL ARTICLE

Effect of stenosis eccentricity on the functionality of coronary bifurcation lesions—a numerical study

Catherine Pagiatakis[1,2] · Jean-Claude Tardif[2,3] · Philippe L. L'Allier[2,3] ·
Rosaire Mongrain[1,2]

Abstract Interventional cardiologists still rely heavily on angiography for the evaluation of coronary lesion severity, despite its poor correlation with the presence of ischemia. In order to improve the accuracy of the current diagnostic procedures, an understanding of the relative influence of geometric characteristics on the induction of ischemia is required. This idea is especially important for coronary bifurcation lesions (CBLs), whose treatment is complex and is associated with high rates of peri- and post-procedural clinical events. Overall, it is unclear which geometric and morphological parameters of CBLs influence the onset of ischemia. More specifically, the effect of stenosis eccentricity is unknown. Computational fluid dynamic simulations, under a geometric multiscale framework, were executed for seven CBL configurations within the left main coronary artery bifurcation. Both concentric and eccentric stenosis profiles of mild to severe constriction were considered. By using a geometric multiscale framework, the fractional flow reserve, which is the gold-standard clinical diagnostic index, could be calculated and was compared between the eccentric and concentric profiles for each case. The results suggested that for configurations where the supplying vessel is stenosed, eccentricity could have a notable effect on and therefore be an important factor that influences configuration functionality.

1 Introduction

Coronary bifurcation lesions (CBLs), defined as luminal narrowings that are in the vicinity of and/or include a significant side branch, constitute up to 20% of all percutaneous coronary interventions (PCIs) [48]. Their intervention is associated with higher rates of peri- and post-procedural clinical events, restenosis, and thrombosis as compared to their isolated counterparts [19, 42, 98]. Interventional cardiologists still rely heavily on angiography for the evaluation of coronary lesion severity, despite its poor correlation with the presence of ischemia [26, 29, 90]. In order to improve the accuracy of the current diagnostic procedures, an understanding of the relative influence of geometric characteristics on the induction of ischemia is required.

For isolated lesions, the onset of ischemia is influenced by various factors including lesion morphology and location, the size and the dynamics of the distal myocardial bed being perfused, and the extent of collateral circulation [62, 67, 68, 100]. The fractional flow reserve (FFR), a dimensionless diagnostic index that quantifies the percent of healthy hyperemic myocardial blood flow that is preserved when the supplying artery

✉ Catherine Pagiatakis
catherine.pagiatakis@mail.mcgill.ca

1   Department of Mechanical Engineering, McGill University, 817
     Sherbrooke Street West, Montreal, Quebec H3A 0C3, Canada

2   Montreal Heart Institute, 5000 Belanger Street,
     Montreal, Quebec H1T 1C8, Canada

3   Faculty of Medicine, Université de Montréal - Pavillon
     Roger-Gaudry, 2900 Edouard-Montpetit Boulevard,
     Montreal, Quebec H3T 1J4, Canada

🙋 Springer

is diseased, is a measure of the hemodynamic (functional) impact of coronary stenoses [83, 100]:

$$FFR = \frac{Q_d}{Q_n} \approx \frac{P_d}{P_{ao}} \tag{1}$$

where Q_d and Q_n are the diseased and theoretical normal flow in the myocardium respectively and P_d and P_{ao} are the distal stenosis pressure and aortic pressure respectively (all at maximum hyperemia, in the absence of microvascular differences between the healthy and diseased states). Clinical studies have shown that pressure-based FFR values between 0.75 and 0.8 correspond to the threshold for the onset of ischemia, and by using FFR to assess the functional impact of coronary lesions, interventions can be safely deferred for physiologically non-significant but angiographically significant lesions [21, 47, 69, 71, 90].

Conversely, the development of ischemia in CBLs is more involved than that of isolated lesions because they are subject to hemodynamic interactions, both on the local level (within the diseased bifurcation) and on the global level (between the different myocardial beds), which render the overall dynamics of the system more complex [20, 28, 29, 45, 48, 70, 99, 104]. To the best of the authors' knowledge, only a recent study by the authors [64], which numerically characterized and compared the FFR between different multilesional configurations at diameter reductions ranging from mild to severe cases using geometric multiscale modelling, considered these hemodynamic interactions and provided an initial clinical perspective into CBLs. In other previous works of CBLs [7, 8, 10–12, 14–16, 27, 103], due to the use of conventional computational fluid dynamics (CFD) simulations, emphasis was put on disease progression rather than functionality.

Furthermore, to date, the effect of anatomical and morphological characteristics of the stenoses and of the arterial bifurcations on CBL hemodynamics has not been systematically investigated. In the aforementioned works, stenoses were modelled by a concentric and axisymmetric profile whereas many studies have shown that an important proportion of coronary bifurcation lesions have eccentric morphology [3, 9, 49, 63, 77, 89], wherein the flow divider is spared of disease [53, 63, 77]. In addition, investigations have demonstrated that a notable percentage of stenoses in the supplying artery display luminal eccentricity; for example, within left main coronary artery (LMCA) bifurcation lesions, Oviedo et al. [63] found that approximately 35% of supplying vessel stenoses were eccentric.

Lesion eccentricity could be an important consideration in CBL functionality as several previous numerical studies have demonstrated the presence of hemodynamic differences, namely regarding the pressure losses, the size of the recirculation zone, and the fluid jet strength and directionality, between eccentric and concentric stenosis profiles for isolated stenoses [37, 38, 72, 101, 102]. However, a functional perspective on the effect of eccentricity, relating to clinical manifestation of the disease, was not provided.

From a clinical perspective, conclusions regarding the effect of eccentricity on the FFR are conflicting. Using in vivo porcine models, Huo et al. [36] demonstrated that isolated lesion eccentricity had a minimal effect on myocardial FFR. Opolski et al. [62] correlated patient-specific plaque morphological parameters to FFR measurements and determined that there was no difference in the average lumen eccentricity between the positive and negative FFR group. Conversely, in a study similar to Opolski et al. [62], Takashima et al. [88] found that FFR was significantly lower, statistically, for eccentric stenosis cases compared to non-eccentric ones.

These studies demonstrate that the effect of lesion eccentricity on the functionality of coronary stenoses is still not well understood. Although clinical studies suggest that eccentricity may not have a dominant effect of coronary lesion functionality compared to other morphological characteristics, isolated stenoses have only been considered to date. As such, the effect of eccentricity on CBL functionality, wherein stenoses are in close proximity to one another and to the flow divider, remains unknown and has not been systematically investigated.

In the current study, it is hypothesized that lesion eccentricity could influence the functionality of CBLs. Thus, the objective was to compare the functional impact, as quantified by the flow-based and pressure-based FFR, between different CBL configurations with eccentric and concentric stenoses. In order to take into account the dynamics of the distal myocardium and to obtain physiologically relevant flow reductions and pressure drops so as to characterize the functionality of the different cases without making any a priori assumptions, CFD simulations are executed under a geometric multiscale framework wherein the truncated 3D vascular domain is numerically coupled to a 0D model of the surrounding cardiovascular structures. This idea allows for flow and pressure fields to develop through the interaction of the two subdomains.

2 Methods

A closed-loop geometric multiscale model consisting of a 3D idealized representation of the bifurcation of the LMCA into the left anterior descending artery (LAD) and the left circumflex artery (LCX) coupled to a 0D model or lumped-parameter model (LPM) of the rest of the cardiovascular system was developed previously [64], as is displayed in Fig. 1. In the current study, the model in Fig. 1 was used as a tool to systematically and comprehensively investigate a clinically measurable parameter that can have clinical consequence and can influence current diagnostic practice. Details pertaining to the individual models are provided in the sections to follow.

Fig. 1 Multiscale model of the bifurcation of the LMCA into the LAD and LCX [64]
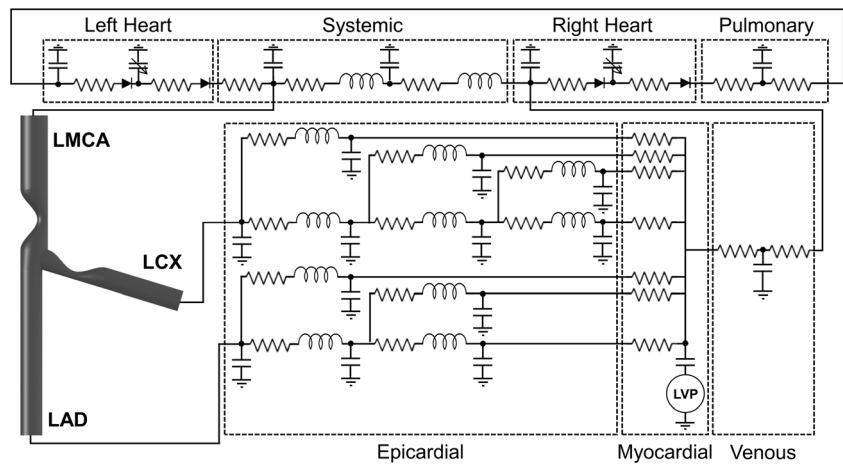
2.1 3D model of the diseased bifurcation

Eight different bifurcation lesion configurations as denoted by the Medina classification [52] were modelled in the study. Clinically, the Medina classification has become widely adopted due to its simplicity [65, 98]. It constitutes a binary system that denotes either the presence (1) or the absence (0) of a stenosis with a diameter reduction greater than 50% in each vessel of the bifurcation as follows: (proximal main vessel, distal main vessel, side branch).

For each modelled case, both eccentric and concentric stenosis profiles were considered and represented using the same cosine curve [101] and circular luminal cross sections. The length of the stenosis was kept constant at 10 mm [64]. Mild, intermediate and severe lesions, with diameter reductions of 41, 50, 61, and 68% were simulated for each configuration. All stenoses within a given configuration had the same severity. As such, including the healthy bifurcation, a total of 57 cases were simulated in the study. Figure 2 provides examples of all the configurations and diameter reductions with both eccentric and concentric stenosis profiles. The dimensions of the native bifurcation were based on average values from the literature [13, 23, 27, 76, 78, 95, 103].

The fluid domain, denoted by Ω, was modelled using the transient, incompressible, and Newtonian Navier-Stokes equations (NSE, Eq. (2)):

$$\begin{cases} \nabla \cdot \overrightarrow{u} = 0 \\ \rho \left(\dfrac{\partial \overrightarrow{u}}{\partial t} + \overrightarrow{u} \cdot \nabla \overrightarrow{u} \right) + \nabla p - \mu \nabla^2 \overrightarrow{u} = 0 \end{cases} \text{on } \Omega \times (0, T) \quad (2)$$

where ρ and μ are the fluid density (1060 kg m^{-3}) and viscosity (0.0035 Pa s) [103], respectively, $\overrightarrow{u}$ and p are the fluid velocity and pressure, respectively, and T is the length of one cardiac cycle (0.8 s).

Studies have shown that blood flow can transition from a laminar to turbulent regime at low Reynolds numbers in stenosed vessels [57, 86, 92]; specifically a threshold Reynolds number of approximately 500 has been suggested for the onset of a transition flow regime, although several studies have demonstrated its initiation at both lower and higher Reynolds numbers [17, 25, 50].

Table 1 displays the instantaneous peak inlet Reynolds number within the LMCA, for all configurations with a stenosis in the supplying artery. The presented Reynolds numbers were calculated based on the native LMCA vessel diameter and the peak instantaneous volumetric flow, for each percent diameter reduction with both eccentric and concentric profiles. Table 2 presents the instantaneous peak inlet Reynolds number within the LMCA for all (0,0,0) configurations with diameter reduction of 41%.

The tables show that the suggested threshold for the transition to turbulence was only significantly surpassed in cases exhibiting up to a 50% diameter reduction; for the concentric stenosis profiles with a 61% diameter reduction, the (1,0,0) and (1,1,0) configurations resulted in Reynolds number just above the threshold (508 and 503, respectively), whereas for
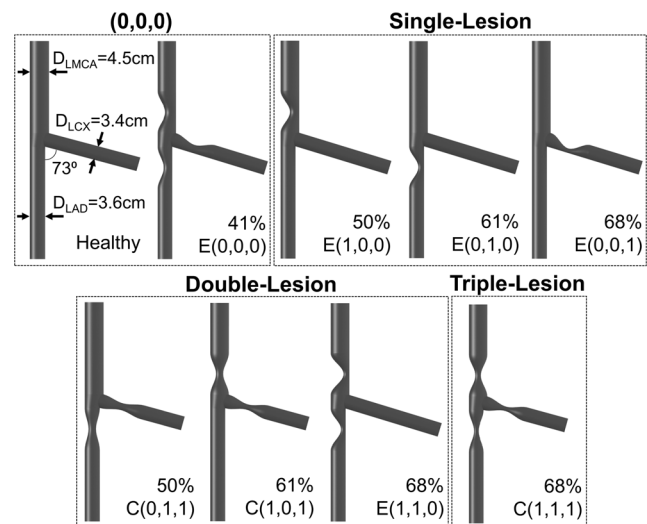

Fig. 2 Eccentric (E) and concentric (C) bifurcation lesion configurations based on the Medina classification that were modelled in the study

Table 1 Peak Reynolds number at the inlet of the LMCA, for each configuration with a supplying vessel stenosis at each and percent diameter reduction, as computed based on the peak inlet LMCA velocity and the native (healthy) LMCA diameter

	Reynolds number [−]					
	Concentric			Eccentric		
	50%	61%	68%	50%	61%	68%
(1,0,0)	573	508	427	563	488	405
(1,0,1)	565	487	406	555	473	390
(1,1,0)	568	503	423	556	472	387
(1,1,1)	560	472	388	546	450	357

the rest of the cases with diameter reductions of 61 and 68%, the Reynolds number was less than 500. The instantaneous peak inlet Reynolds number within the LMCA decreased with increasing stenosis severity due to the fact that the total flow to the left coronary tree was correspondingly decreasing with an increase in the epicardial resistance. Since the suggested threshold for the onset of a transitional flow regime was surpassed for mild-moderate diameter reductions, a laminar flow regime was assumed within the study. The incorporation of a turbulent regime would require a significant refinement of the spatial discretization, thus resulting in an increase in computational time [4, 93]. This assumption was therefore important due to the parametric nature of the work, as well as the increase in computational time resulting from the multiscale algorithm. Furthermore, studies have shown that many turbulence schemes available in commercial software packages, such as ANSYS Fluent, are still unable to accurately capture low Reynolds number transition to turbulence characteristics in post-stenotic regions [39, 93]; as such, due to the uncertainty in turbulence modelling for such applications, the increased computational time and the retrospective quantification of the Reynolds number, the application of a laminar flow regime was justified for the scope of the work.

The mathematical model was initialized with conditions at time $t = 0$ on the velocity, namely $\overrightarrow{u} = \overrightarrow{u}_0$. The initial conditions were obtained from a steady-state solution wherein average pressures, obtained from the solution of the full LPM of the healthy case, were applied as boundary conditions (BCs). As studies have shown that diseased

coronary vessels are subjected to peak circumferential strains less than 5% [40, 85], the vessel walls were modelled as being rigid and a no-slip condition was applied. Details regarding the boundary conditions on Γ_{LMCA}, Γ_{LAD}, and Γ_{LCX} are provided in subsequent sections; these boundaries serve as interfaces between the 3D and 0D model, and therefore, their conditions are dependent on the mathematical formulation of the 0D model.

2.2 0D model of the rest of the cardiovascular system

0D models allow for the global dynamics of large and complex vascular domains to be modelled in a computationally efficient manner through the use of electrical analogue components. The electrical analogue employed in the study can be found in [64], which was developed based on existing models in the literature. It consists of models of the heart, systemic and pulmonic circulations, and the epicardial, myocardial, and venous left coronary circulations.

The coronary model was based primarily on the coronary map provided in PCI guidelines [80] and the models of Pietrabissa et al. [66] and Wang et al. [95]. Each epicardial artery was represented by a three-element Windkessel (WK) model consisting of a resistance (R), inductance (L), and capacitance (C). Expressions for the calculation of the RLC parameters are provided in Eq. (3), as derived by linearizing and spatially averaging the NSE:

$$R = \frac{128\mu l}{\pi D^4} \qquad L = \frac{4\rho l}{\pi D^2} \qquad C = \frac{\pi D^2}{4} C_{norm} \qquad (3)$$

where l is the vessel length [cm] and D the vessel diameter [cm]. In order to eliminate assumptions regarding the material model and the thickness of the vessel wall, the volumetric arterial compliance (C) was calculated based on an average in vivo distensibility, C_{norm} [mmHg^{-1}], which was assigned a value of 0.002 mmHg^{-1} from the literature [1, 40, 85, 97]. Epicardial geometric data and the corresponding parameter values utilized in the model can be found in [64].

Since the microcirculation provides the majority of the resistance to flow in the coronary arteries, the circulation downstream each of the terminal epicardial arteries was modelled using a single simple terminal resistance through which hyperemic conditions were implemented. Specifically, the total

Table 2 Peak Reynolds number at the inlet of the LMCA for the (0,0,0) configurations with stenoses of 41% diameter reduction. The values are computed based on the peak inlet LMCA velocity and the native (healthy) LMCA diameter.

	Reynolds number [−]			
	(41%, 0, 0)	(41%, 0, 41%)	(41%, 41%, 0)	(41%, 41%, 41%)
Concentric	596	591	594	586
Eccentric	591	587	587	583

hyperemic myocardial resistance of the left coronary tree was estimated by assuming a linear relationship between the pressure drop and the flow:

$$\Delta P_{\mathrm{myo}} = R_{\mathrm{tot}} Q_{\mathrm{tot}} \tag{4}$$

where ΔP_{myo} is the total average myocardial pressure drop and R_{tot} and Q_{tot} are the total average hyperemic myocardial resistance and flow, respectively. Q_{tot} was taken to be 5 ml s^{-1} (assuming an average resting flow of 1 ml s^{-1} [16, 103] and a coronary flow reserve (CFR) of 5.0 [29]) and ΔP_{myo} was assigned a value of 91 mmHg (based on average aortic and venous pressures of 96 and 5 mmHg, respectively). Therefore, R_{tot} was calculated to be 18 mmHg s ml^{-1}. The value of each terminal resistance was estimated by scaling R_{tot} based on the diameter of the terminal epicardial artery D_{term} and the supplying artery D_{LMCA}, using allometric scaling laws developed by Huo et al. [34, 35].

Left coronary flow is out of phase with aortic flow due to systolic left ventricular contraction wherein intramyocardial pressure is high, endocardial coronary vessels are compressed, and thus perfusion is hindered. Consequently, the majority of left myocardial perfusion occurs during diastole. In order to globally model this phenomenon, a single myocardial compliance was coupled to a pressure generator with equal magnitude and phase as left ventricular pressure.

The systemic circulation was subdivided into models of the aortic sinus and aorta (four-element WK) and the peripheral arterial system (three-element WK) based on [2, 51]. A simple three-element WK model based on [41] was implemented for the pulmonic circulation. Left and right ventricular contraction were modelled using time-varying elastance functions. Time-varying elastance is defined as the ventricular pressure-volume ratio; when the curve is normalized with respect to the maximum elastance (E_{max}) and the time at which the maximum elastance occurs ($t_{E\mathrm{max}}$), it is constant between patients [81, 84]. Therefore, in the heart models of the current study, the normalized curve was scaled using average E_{max} and $t_{E\mathrm{max}}$ from the literature [41, 81] for both the left and right ventricles. A passive model for the atria, consisting of constant elastances, and linear models of the heart valves were implemented in order to simplify numerics [41, 46, 81]. Details about the parameter values for the heart, systemic, and pulmonic models that were implemented in the model can be found in [64].

Mathematically, each basic vascular compartment of the 0D model (consisting of a single RCL unit, as is displayed in Fig. 1 for each epicardial coronary artery) is represented by the linearized and spatially averaged NSE (Eq. (5)) [56]:

$$C \frac{dp_{\mathrm{out}}}{dt} = Q_{\mathrm{in}} - Q_{\mathrm{out}}$$
$$L \frac{dQ_{\mathrm{in}}}{dt} = -RQ_{\mathrm{in}} + p_{\mathrm{in}} - p_{\mathrm{out}} \tag{5}$$

where Q_{in} and Q_{out} are the time-dependent average inlet and outlet flow rates, respectively, and p_{in} and p_{out} are the time-dependent average inlet and outlet pressures, respectively. When several basic compartmental units are combined, the complete system is modelled by a differential-algebraic equation, which with the appropriate algebraic substitutions converts to the system of ordinary differential equations (ODEs) given in Eq. (6):

$$\frac{d\bar{y}}{dt} = A\bar{y} + \bar{b} \tag{6}$$

where $\bar{y}$ is a vector of unknown nodal flows and pressures (state variables), A is a square matrix of parameter values, and $\bar{b}$ is a column vector of forcing terms obtained from the 3D model. Details regarding the column vector of forcing terms, which serves as the interface between the 0D and 3D models, are provided in subsequent sections.

2.3 Multiscale algorithm for 3D-0D model coupling

Numerical coupling between heterogeneously dimensioned models can be accomplished through either monolithic [94] or partitioned [74, 75] approaches. The monolithic approach requires significant changes to the flow solver [24], whereas the partitioned approach allows relatively complex 0D models to be implemented and commercial software to be used. Therefore, a partitioned approach based on the work of Quarteroni et al. [74, 75] was selected for the coupling between the 3D and 0D models. Fundamentally, the coupling consists of the enforcement of stress and flux continuity at each of the interfaces between the two models, which therefore governs the forcing terms in the 0D model (column vector $\bar{b}$, Eq. (6)) and the boundary conditions applied in the 3D model. However, this formulation results in defective boundary conditions due to the fact that the NSE require point-wise boundary data to ensure well-posedness whereas the 0D model only provides spatially averaged data. The treatment of defective boundary conditions was addressed in the work of Heywood et al. [32] who demonstrated that such BCs are treated implicitly with an extended variational formulation of the NSE, specifically, through the weak fulfillment of the Neumann BC. Proof of well-posedness as well as a more detailed mathematical description of the geometric multiscale formulation can be found in [32, 74, 75].

The boundaries Γ_{LMCA}, Γ_{LAD}, and Γ_{LCX} of the 3D model were interfaced with the 0D model through capacitances; therefore, Neumann stress BCs were applied as BCs in the 3D bifurcation lesion models:

$$p_i \hat{n}_i - \mu \nabla \vec{u}_i \cdot \hat{n}_i = p_j(t) \hat{n}_i \tag{7}$$

for any cell face i on boundary j = LMCA, LAD, and LCX and where $\hat{n}_i$ is the surface normal, $\vec{u}_i$ is the velocity, and $p_j(t)$ is the time-dependent average pressure. However, it can be

shown that when a given planar boundary j is perpendicular to a cylindrical segment, the boundary condition given by Eq. (7) reduces to the following [32]:

$$p_i \hat{n}_i = p_j(t)\hat{n}_i \qquad (8)$$

Therefore, average, uniform, time-dependent pressures (or conversely normal stresses) were applied at each of the boundaries of the 3D geometry and the solution of the 0D model was forced by average flows obtained from the 3D model, at each of the boundaries, such that the column vector $\overline{b}$ in Eq. (6) was given by:

$$\overline{b} = [\dots \ Q_{LMCA} \ \dots \ Q_{LAD} \ \dots \ Q_{LCX} \ \dots]^T \qquad (9)$$

where

$$Q_j = \int_{\Gamma_j} \overrightarrow{u} \cdot \hat{n} d\gamma \qquad (10)$$

for j = LMCA, LAD, and LCX and $\overrightarrow{u}$ obtained from the 3D model.

2.4 Numerical implementation of the multiscale model

The transient 3D flow simulations were solved using the commercial software package ANSYS Fluent (Canonsburg, PA, USA). A fourth-order Runge-Kutta method within an in-house subroutine written in C++ was employed for the solution of the nonlinear system of ODEs describing the dynamics of the 0D model. Its solution was coupled to the NSE within ANSYS at each timestep using a fully automated external user-defined function written in C.

An explicit, staggered approach over the cardiac cycle $(0,T)$ was used for the coupling; at each time step (t^n, t^{n+1}) with $t^{n+1} = t^n + \Delta t$, the boundary pressures at time t^{n+1} were initially solved for by forcing the solution of the ODE system with the average boundary flow rates obtained from the 3D model at the previous timestep:

$$Q_i^{t_{n+1}} = \int_{\Gamma_i} \overrightarrow{u}^{t_n} \cdot \hat{n} d\gamma \qquad (11)$$

The calculated boundary pressures were then applied to the 3D model in order calculate the 3D velocity and pressure fields, as well as the average flow rate at each of the boundaries at time t^{n+1}. The average flow rates in turn forced the solution of the ODE system at the next time step.

The 3D geometries were meshed within ANSYS. A mesh sensitivity analysis was executed for the (1,1,1) and (1,1,0) configurations with a 68% diameter reduction. More specifically, three mesh densities were considered: ~135,000 elements (coarse), ~250,000 elements (medium), and ~520,000 elements (fine). Six cycles were executed for each simulation to ensure that transient effects had been eliminated. The parameters used to assess mesh convergence were the average

boundary pressures and the average boundary flows, based on similar studies employing geometric multiscale models [4, 5, 33, 44, 79]. Details regarding the mesh sensitivity analysis can be found in [64]. The final meshes had an approximate mesh density of 170,000 elements.

3 Results

CFD simulations of different CBL configurations with concentric and eccentric stenosis profiles of varying severity were executed under a multiscale framework. Spatially and temporally averaged pressures and flows at each of the boundaries of the bifurcation were computed and employed in the calculation of the flow-based and pressure-based FFR, which allowed for a functional perspective on the effect of lesion eccentricity on CBLs to be obtained. The findings are reported in regard to the effect of luminal eccentricity in the clinical manifestation of the disease, rather than in the context of the validity of the model developed previously in [64].

3.1 Flow and pressure profiles

Figure 3a, b displays the flow and pressure, respectively, at the boundaries of the healthy 3D model. The average LMCA, LAD, and LCX flows were 4.39, 2.15, and 2.23 ml s^{-1}, respectively.

The average aortic, distal LAD, and distal LCX pressures were 98.7, 97.5, and 96.9 mmHg, respectively, which yielded a healthy pressure-based FFR of 0.99 and 0.98 for the LAD and the LCX, respectively.

Figure 3c, e displays the time-dependent flow in the LAD and LCX, respectively, for the (1,0,0) configuration with eccentric stenosis profiles for varying diameter reduction. As the stenosis severity increases, the amplitude and therefore the cycle-averaged flow rates decrease within each of the vessels. The amplitude of the time-dependent LAD and LCX pressure curves (subpanels d and f, Fig. 3, respectively) also decrease as the percent diameter stenosis increases. Similar curves are obtained for all diseased cases.

3.2 Flow-based FFR

Figure 4 compares the flow-based FFR in the LAD and LCX between the eccentric and concentric stenosis profiles within the single-lesion configurations. The left-hand panel displays the computed FFR values, while the right-hand panel presents the corresponding percent differences in FFR between the two profiles relative to the concentric case at each diameter reduction. In the (1,0,0) configuration, a decrease in LAD FFR is observed for the eccentric case relative to the concentric one. The maximum decrease, occurring at the most severe diameter reduction, is 10.5%. Conversely, in the LCX, the eccentric

Fig. 3 **a** Flow and **b** pressure in the healthy bifurcation. *Dotted lines* correspond to the cycle-averaged values. Flow in the **c** LAD and **e** LCX and pressure in the **d** LAD and **f** LCX for the (1,0,0) configuration with eccentric stenosis profiles and varying severity
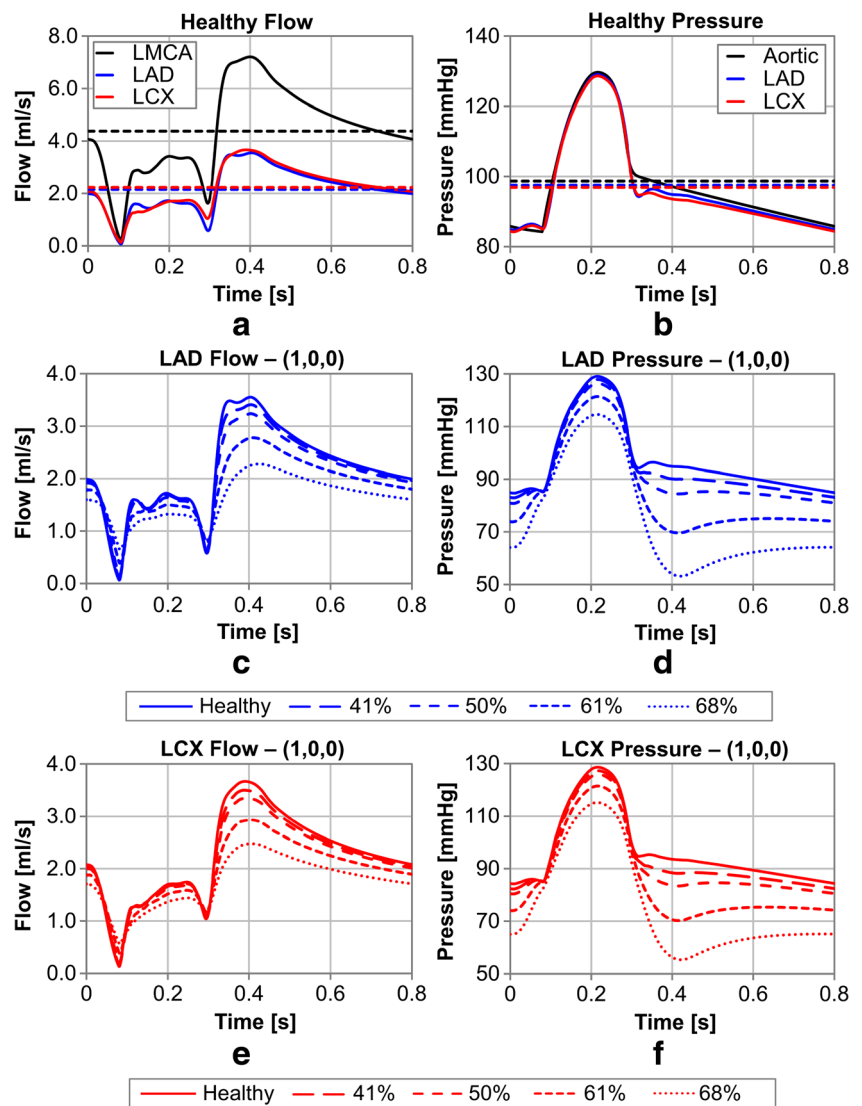

profile displays an increase in FFR relative to the concentric case; the corresponding maximum difference is below 5%. For the (0,1,0) and (0,0,1) configurations, within the LAD and LCX, respectively, the FFR is lower for the eccentric case compared to the concentric profile. In both configurations, the maximum difference remains below 4%. The maximum percent differences between the eccentric and concentric profiles for the single-lesion configurations are summarized in Table 3.

Figure 5 compares the flow-based FFR in the LAD and LCX between eccentric and concentric stenosis profiles for the multilesional configurations. A lower FFR is observed for the eccentric case compared to its concentric counterpart in both the LAD and LCX in the (0,1,1) configuration (Fig. 5a, b). This configuration is the only multilesional case without a stenosis in the supplying artery; similarly to the single daughter vessel lesion configurations (Fig. 5c–f), the maximum percent difference between the two cases is small (less than 2.0% within both daughter vessels). Conversely, for all multilesional

cases with a stenosis in the LMCA, a substantial decrease in LAD FFR is computed; in the LCX, the FFR for the eccentric case is higher than that of the concentric profile. The maximum differences in FFR between the eccentric and concentric cases for the (1,0,1), (1,1,0) and (1,1,1) configurations occur within the LAD and are 10, 16, and 14%, respectively. The corresponding increase in FFR within the LCX was 8.1, 6.9, and 8.0% for the same configurations, respectively. The maximum percent differences between the eccentric and concentric profiles for the multilesional cases are summarized in Table 3.

Figure 6 displays the velocity contours near the bifurcation carina in the (1,0,0) configuration with a stenosis of 50% for both the concentric and eccentric stenosis profiles at time $t = 0.7$ s. It can be observed that for the concentric case, the emerging jet is centered at the axis of the vessel, whereas for the eccentric case, it shifted towards the wall of the vessel opposite the stenosis. Furthermore, in the concentric case, the velocity in the LAD is higher than it is in the LCX.

Fig. 4 Comparison of the flow-derived FFR in the LAD and LCX for the **a** (1,0,0), **c** (0,1,0), and **e** (0,0,1) configurations between concentric (C) and eccentric (E) stenosis profiles. Percent differences (Diff) between the concentric and eccentric flow-based FFR in the LAD and LCX for the corresponding configurations are shown in **b**, **d**, and **f**
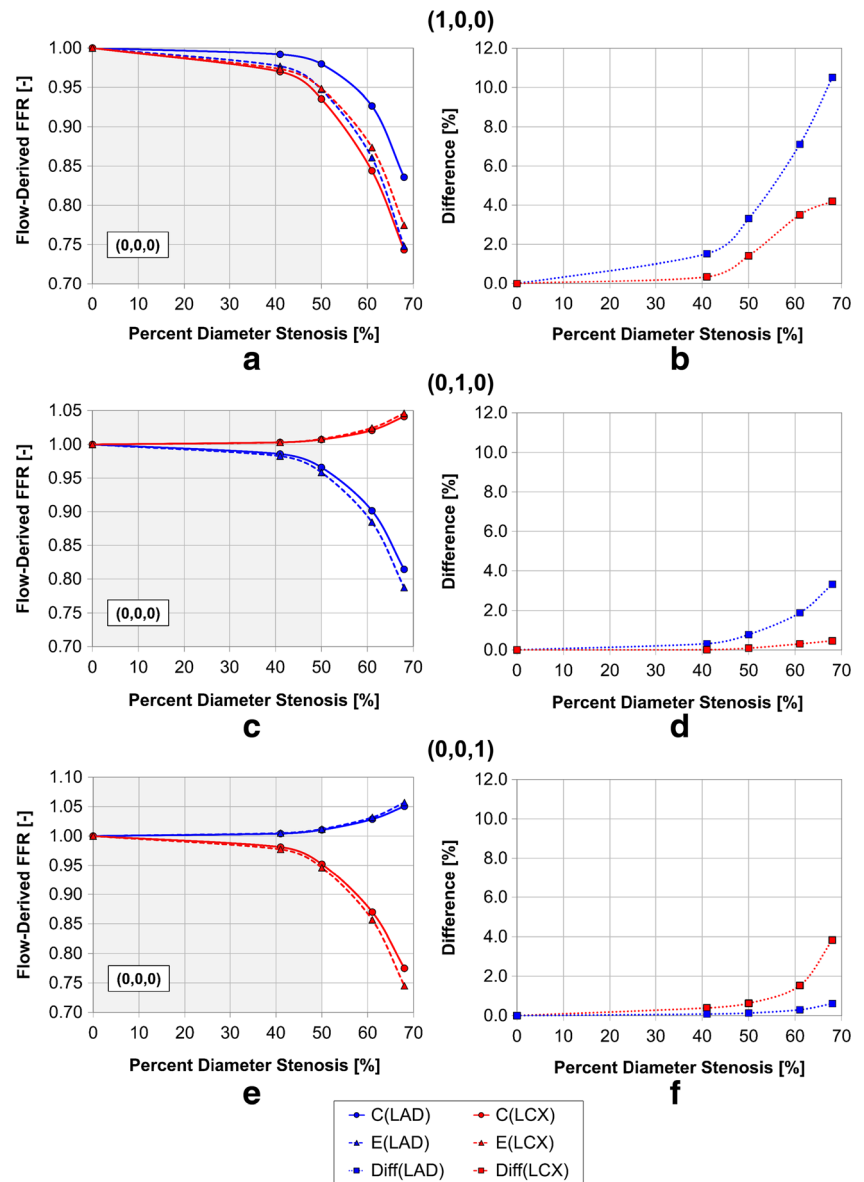
Conversely, in the eccentric case, the flow appears to be distributed more equally between the two daughter vessels, with a noticeably weaker jet being observed in the LAD.

3.3 Pressure-based FFR

Figure 7 displays the pressure-based FFR in the LAD and the LCX for each multilesional configuration for both the eccentric and concentric cases. The trends observed for the pressure-derived FFR are similar to those observed for the flow-derived FFR. Specifically, for the multilesional cases with a stenosis in the supplying artery, a decrease in LAD FFR and an increase in the corresponding LCX FFR are observed for the eccentric stenosis profiles relative to the concentric cases. However, the magnitude of the differences in the pressure-based FFR is smaller than those computed for the flow-based FFR. Specifically, in

the (1,0,1), (1,1,0), and (1,1,1) configurations, the maximum differences are 7.3, 11, and 10%, respectively. The maximum percent difference in the pressure-based FFR between the eccentric and concentric stenosis profiles within the LAD and LCX for all configurations is provided in Table 3.

4 Discussion

Clinical studies have shown that coronary stenoses tend to be eccentric; yet, to the best of the authors' knowledge, the effect of eccentricity on stenosis functionality, specifically in the case of CBLs, has not been systematically investigated. Therefore, CFD simulations of different CBL configurations with both eccentric and concentric stenosis profiles were executed under a geometric multiscale framework using a model

Table 3 Maximum percent difference in the flow- and pressure-based FFR within the LAD and LCX between the eccentric and concentric stenosis profiles, relative to the concentric case

		Maximum difference [%]			
		Flow-based FFR		Pressure-based FFR	
		LAD	LCX	LAD	LCX
Single-lesion	(1,0,0)	10.5	4.2	7.7	1.5
	(0,1,0)	3.3	0.46	2.4	1.5
	(0,0,1)	0.61	3.8	0.0026	2.7
Multi-lesion	(0,1,1)	2.0	1.5	1.8	1.5
	(1,0,1)	10.1	8.1	7.3	4.1
	(1,1,0)	15.8	6.9	11.1	2.9
	(1,1,1)	14.3	8.0	10.3	3.2

developed in a previous study [64]. With the use of a multiscale model, it was possible to investigate the effect of lesion eccentricity from a functional perspective based on the gold-standard clinical index (FFR). More specifically, by coupling the 3D model to a 0D model of the rest of the cardiovascular system, the need to assume and apply arbitrary boundary conditions was eliminated and flow and pressure within the 3D model were allowed to develop for the different configurations through the interaction between the two models such that the resulting profiles were physiologically realistic.

4.1 Flow and pressure profiles

A justification of the computed flow and pressure curves for the healthy case has been provided in [64] but is described briefly here based on the corresponding values of FFR. More specifically, the computed FFR values in the simulated configurations are in good accordance with values reported in the literature for similar stenosis severity ranges. With reference to Figs. 4 and 5, for diameter reductions between 61 and 68%, the FFR in the LAD ranged between 0.64 and 0.95 while the FFR in the LCX ranged between 0.61 and 0.90. More specifically, 50% of the investigated cases within the aforementioned stenosis severity range had FFR values below 0.8, with 41% of these cases having an FFR below 0.75. Takagi et al. [87] reported FFR values ranging between 0.35 and 0.75 for diameter reductions between 60 and 80%. Hamilos et al. [31] measured FFR values between 0.68 and 0.97 for stenoses with severities between 60 and 70%, and Meimoun et al. [54] determined a range of FFR values between 0.68 and 0.76 for stenoses with diameter reductions of about 70%. Furthermore, Fischer et al. [26] reported that of all stenoses with diameter reductions greater than 60%, only 38% had FFR values less than 0.75 while Koo et al. [43] found that for an average diameter reduction of 79 ± 11% the average FFR was 0.81 ± 0.12 with only 31% of lesions having

an FFR below 0.75. Consequently, the FFR values computed in this study agree well with clinical measurements.

4.2 Comparison of FFR between eccentric and concentric stenoses

The numerical simulations yielded differences in flow- and pressure-derived FFR between the eccentric and concentric stenosis profiles up to 3.8% for the configurations comprising of lesions only within the daughter vessel ((0,1,1), (0,1,0), and (0,0,1)). These configurations are the most representative of isolated lesion cases as there are no proximal or distal stenoses with which they immediately interact; for all these aforementioned cases, the FFR was lower in the eccentric cases compared to the concentric ones which signifies that eccentric stenoses are associated with higher pressure losses. Higher pressure losses for eccentric stenosis profiles relative to concentric ones have been suggested previously in the literature, for example through in vitro methods by Young and Tsai [101, 102] in isolated straight vessels and by Poepping et al. [72] within carotid bifurcation models. Similarly, in idealized numerical models of isolated concentric and eccentric constrictions within the right coronary artery and LAD, Guleren [55] demonstrated a consistently greater pressure drop during both systole and diastole for lesions with eccentric lumens. Clinically, Takashima et al. [88] demonstrated that FFR values were approximately 6% lower for eccentric cases compared to non-eccentric ones. Therefore, the decrease in FFR recorded in the present study is in good accordance with other literature works.

However, the magnitude of both the computed percent and absolute differences in FFR between the eccentric and concentric cases must be noted; the recorded maximum 3.8% difference corresponded to a maximum absolute difference of 0.03 in the FFR values. In clinic, De Bruyne et al. [22] recorded a coefficient of variance (95%) of 4.8% (mean absolute difference of 0.01 ± 0.04) between successive FFR measurements, which correlated well with differences observed by Berry et al. [6] (absolute differences of 0 ± 0.04). Consequently, the FFR differences between eccentric and concentric profiles presented in the current study for isolated lesions fall within the reported clinical variance. Interestingly, these observations are in line with several clinical studies that have shown that lesion eccentricity does not play a dominant role in the isolated coronary lesion functionality [36, 62].

Configurations with a supplying vessel stenosis showed markedly different behavior from those with a healthy LMCA. More specifically, a decrease in LAD FFR and an increase in LCX FFR were observed for the eccentric profiles relative to the concentric ones. In the LAD, the maximum decrease in flow- and pressure-based FFR ranged between 10 and 16% and between 7 and 11%, respectively; in the LCX, the maximum increase in FFR ranged between 4 and 9% and between 1.5 and 4.1%, respectively. The smaller

Fig. 5 Comparison of the flow-derived FFR in the LAD and LCX for the **a** (0,1,1), **c** (1,0,1), **e** (1,1,0), and **g** (1,1,1) configurations between concentric (*C*) and eccentric (*E*) stenosis profiles. Percent differences (*Diff*) between the concentric and eccentric flow-based FFR in the LAD and LCX for the corresponding configurations are shown in **b**, **d**, **f**, and **h**
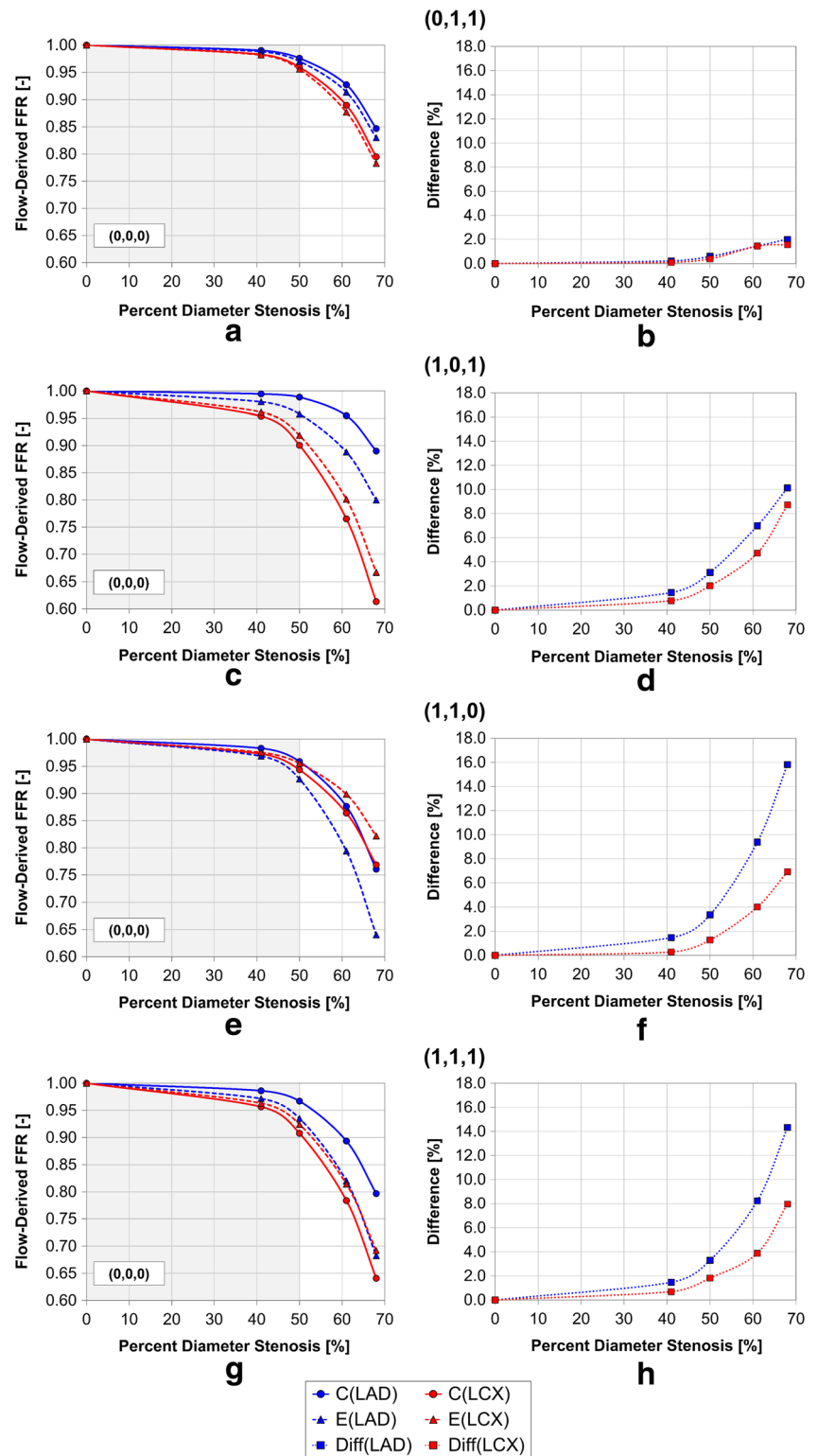
differences for the pressure-based FFR compared to the flow-based on can be attributed to the fact that zero compliance is assumed in the derivation of pressure-based FFR, whereas the present model did not disregard compliance. Furthermore, the magnitude of the decrease in LAD FFR was greater than the corresponding increase in LCX FFR, suggesting that eccentricity has a nonlinear effect on the daughter vessel functionality. The corresponding maximum absolute changes in flow-based FFR within the LAD and LCX were 0.09–0.12 and 0.03–0.05, respectively. Consequently, in particular within the LAD, the
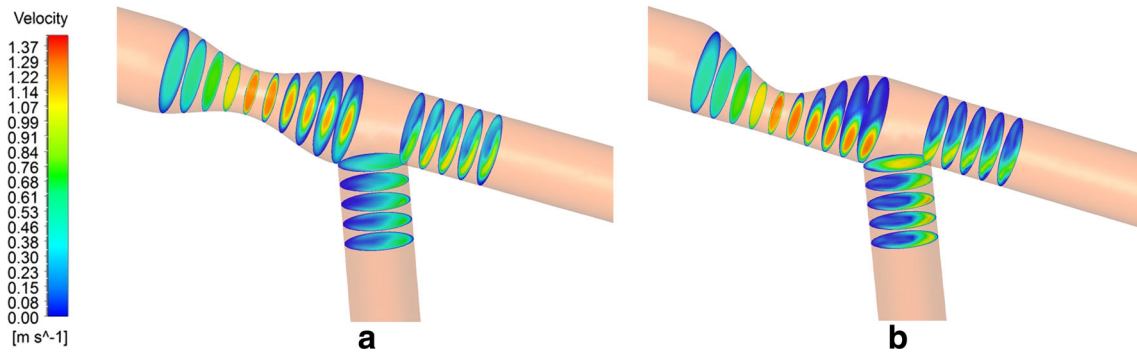
Fig. 6 Velocity contours in the (1,0,0) configuration with a 50% diameter reduction for the **a** concentric and **b** eccentric profiles at t = 0.7 s

absolute changes in FFR computed in the current study notably surpassed the reported variance associated with clinical FFR measurements [6, 22]; for severe diameter reductions, the differences in LCX were also above clinical variance ranges.

The decrease in LAD FFR in conjunction with the increase of the LCX FFR between the concentric and eccentric stenosis profiles can be attributed to the offset of the supplying vessel stenosis jet in the eccentric case relative to the concentric one. In the case of the eccentric profile, the high momentum jet emerging from the neck of the supplying vessel stenosis was shifted towards the bifurcation carina which permitted more flow to be diverted to the LCX compared to the concentric profile case where the emerging jet was directed towards the lumen of the LAD. Jet skewness in eccentric constrictions has been previously reported in numerical and in vitro studies for various eccentricity indices in both straight [30, 37, 55, 92]

and bifurcating vessels [72]. Therefore, the results presented in this study are in accordance with literature.

The results of the study suggest that the altered hemodynamics, including emerging jet skewness, induced distal to stenoses with luminal eccentricity may have a minor impact on the translesional pressure drop and thus the functionality of lesions that are not in close proximity to and not proximal to other lesions and vessel bifurcations, for example in the (0,1,0), (0,0,1), and (0,1,1) configurations. Conversely, when a stenosis is located near and proximal to a bifurcation carina, as was the case for the supplying vessel stenosis in the (1,0,0), (1,0,1), (1,1,0), and (1,1,1) configurations presented in the current study, the flow patterns distal to the lesions overlap and therefore closely interact with the flow divider. As such, altered hemodynamics induced by eccentricity of the stenosed proximal lumen could have a substantial influence on the flow

Fig. 7 Comparison of pressure-derived FFR between concentric (C) and eccentric (E) stenosis profiles in the LAD and LCX for the **a** (0,1,1), **b** (1,1,1), **c** (1,1,0), and **d** (1,0,1) configurations
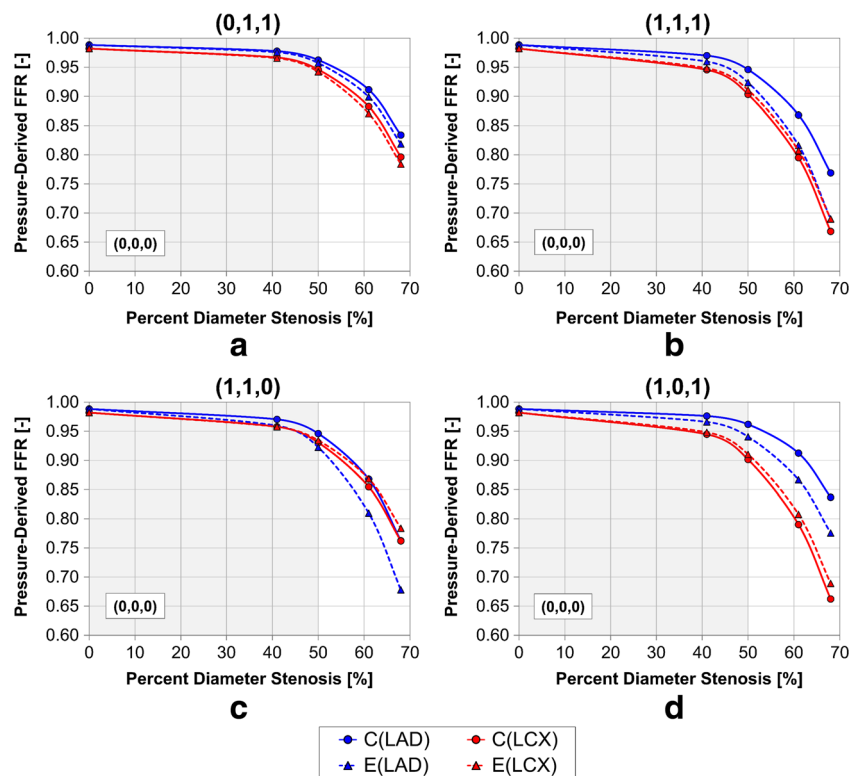
within the individual daughter vessels and thus have an effect of the functionality of the configuration.

4.3 Potential clinical implications

The results discussed have potentially significant clinical implications, which are stated within the limitations of the study, as provided below. The findings suggest that for isolated stenoses, in particular cases that are not proximal to a bifurcation, the effect of eccentricity on lesion functionality is within clinical measurement error and therefore could be negligible; consequently, for isolated lesions, eccentricity may not be an independent/dominant determinant of hemodynamic impact. This idea has been suggested in clinical studies [62], although, to the best of the authors' knowledge, a systematic numerical investigation demonstrating this behavior had not been executed to date. Conversely, for CBL configurations wherein the mother vessel is diseased, the directionality of the supplying vessel stenosis jet, as is influenced by the eccentricity of the corresponding stenosis lumen, could have a notable effect on the distribution of blood between the daughter vessels and thus influence the clinical manifestation of the disease.

An understanding of the geometric factors that influence the functionality of CBLs, such as luminal eccentricity, could ultimately improve diagnostic procedures and thus help reduce treatment risk. More specifically, despite the designation of FFR as the gold-standard in clinical diagnosis for coronary lesions, it is utilized in less than 10% of all catheterization labs prior to intervention [47, 58, 59]. The computation of FFR using multiscale numerical methods (HeartFlow Inc., etc. [61]) is increasing in popularity, yet there is much uncertainty and reservation in its clinical use. As such, interventional cardiologists still heavily rely on an angiographic evaluation of the severity of coronary lesions, which has been shown to have a poor correlation with ischemic considerations [96]. Angiographic evaluations are particularly hindering in the case of bifurcation lesions, where, due to complex geometry, accurate visualization is rendered difficult [48]. There are attempts to derive non-invasive diagnostic indices that could predict, using angiographic parameters, the presence of a hemodynamically critical stenosis; however, such indices require an evaluation of morphological and geometric parameters of both the stenoses and the arteries and an understanding of their relative contribution to the induction of ischemic conditions [60]. The findings of the current study imply that, in close proximity to a bifurcation carina, lumen eccentricity of the supplying vessel could be an influencing factor in CBL functionality.

4.4 Limitations

In vivo, coronary geometry is curved and tortuous [91, 105]; in the current study, linear and planar geometries of the LMCA bifurcation were utilized. While a more realistic (patient-specific) geometry could potentially provide a more accurate representation of the in vivo flow environment, coronary vascular geometry varies significantly from patient to patient; as such, by using a controlled and simplified computer-generated geometry, it was possible to isolate the effect of stenosis profile (eccentric versus concentric) on the functional impact of CBLs, without influencing the results by patient-specific flow patterns. In addition, inertial pressure losses rather than viscous effects (which are most significantly influenced by vessel curvature) are expected to dominate in the translesional pressure drop as a result of the substantial diameter reductions and the hyperemic flow conditions. Consequently, as the resulting flow and pressure profiles were in good accordance with clinical reports, the use of simplified geometries was justified for the scope of the current work. Moreover, coronary arteries are subjected to dynamic motion as a result of the ventricular contraction. This phenomenon was not considered in order to reduce computational costs. Its exclusion from the current model was justified by the fact that in the proximal epicardial coronary arteries, as were modelled in the current study, regions of small curvature changes have been shown to exist [18]; furthermore, flow disturbances induced by bifurcations have been shown to have a dominant effect on flow patterns compared to disturbances generated by dynamic curvature changes [73]. In addition, all stenoses in a given configuration were modelled to be equal in severity. While future works will consider relative stenosis severities, this simplification was employed in the current study so as to isolate the effect of lesion eccentricity on CBL functionality. Finally, with respect to biophysical phenomena, the current study did not incorporate collateral flow. The overall configuration, extent, and response of collaterals to maximum vasodilation vary significantly between patients and are still not fully understood. Moreover, studies have shown that collateral circulation is only present in approximately 30% of patients that have functionally significant coronary lesions [82]. Therefore, the disregard of collateral circulation was deemed acceptable for the scope of the current study. Furthermore, both the downstream epicardial arteries and the microvasculature were assumed to be free of disease. Disease of the downstream epicardial arteries would impose additional resistance in the epicardial tree, thus contributing to the overall flow reduction and ultimately masking the true hemodynamic severity of the upstream bifurcation lesion configuration. Microvascular disease increases the overall myocardial resistance; not only does this signify that under induced hyperemic conditions, total microvascular vasodilation is inhibited, but also that the increased resistance of the microvasculature itself reduces perfusion. Therefore, the true functionality of an epicardial stenosis is underestimated. The presence of peripheral coronary artery disease was disregarded in order to elucidate the true hemodynamic severity of the bifurcation lesion

configurations and to isolate the effect of each of the investigated geometric parameters on the corresponding FFR.

5 Conclusion

CFD simulations employing a geometric multiscale algorithm were executed for single-, double-, and triple-lesion CBL configurations within the LMCA bifurcation. Under the geometric multiscale framework, flow- and pressure-derived FFR could be computed and used to characterize the functionality of the different cases. Both concentric and eccentric profiles for stenoses ranging between mild and severe diameter reductions were considered in order to investigate the effect of lesion eccentricity on the functional impact of the CBLs. To the best of the authors' knowledge, the current study was the first to systematically investigate the effect of lesion eccentricity from a functional perspective. Overall, the results were in good accordance with clinical observations. More specifically, the study found that eccentricity had a negligible effect on the functionality of isolated lesions. Conversely, for CBLs wherein the supplying vessel is stenosed, eccentricity was found to have a notable effect on the FFR of the two daughter vessels; these findings were attributed to the change in directionality of the jet emerging from the supplying vessel stenosis between the concentric and eccentric cases in conjunction with the close proximity of the lesions to the carina. Therefore, from a clinical perspective, these results suggest that luminal eccentricity could be geometric parameter that influences the functionality of CBLs.

References

1. Alfonso F, Macaya C, Goicolea J, Hernandez R, Segovia J, Zamorano J, Banuelos C, Zarco P (1994) Determinants of coronary compliance in patients with coronary artery disease: an intravascular ultrasound study. J Am Coll Cardiol 23(4):879–884. doi:10.1016/0735-1097(94)90632-7

2. Avanzolini G, Barbini P, Cappello A, Cevenini G (1988) CADCS simulation of the closed-loop cardiovascular system. Int J Biomed Comput 22(1):39–49. doi:10.1016/0020-7101(88)90006-2

3. Badak O, Schoenhagen P, Tsunoda T, Magyar WA, Coughlin J, Kapadia S, Nissen SE, Tuzcu EM (2003) Characteristics of atherosclerotic plaque distribution in coronary artery bifurcations: an intravascular ultrasound analysis. Coron Artery Dis 14(4):309–316. doi:10.1097/01.mca.0000076511.29238.fl

4. Balossino R, Pennati G, Migliavacca F, Formaggia L, Veneziani A, Tuveri M, Dubini G (2009) Computational models to predict stenosis growth in carotid arteries: which is the role of boundary conditions? Comput Methods Biomech Biomed Engin 12(1):113–123. doi:10.1080/10255840903080802

5. Baretta A, Corsini C, Yang W, Vignon-Clementel IE, Marsden AL, Feinstein JA, Hsia TY, Dubini G, Migliavacca F, Pennati G, Modeling of Congenital Hearts Alliance I (2011) Virtual surgeries in patients with congenital heart disease: a multi-scale modelling test case. Phil Trans R Soc A 369(1954):4316–4330. doi:10.1098/rsta.2011.0130

6. Berry C, van 't Veer M, Witt N, Kala P, Bocek O, Pyxaras SA, JD MC, Fearon WF, Barbato E, Tonino PA, De Bruyne B, Pijls NH, Oldroyd KG (2013) VERIFY (VERification of Instantaneous Wave-Free Ratio and Fractional Flow Reserve for the Assessment of Coronary Artery Stenosis Severity in EverydaY Practice): a multicenter study in consecutive patients. J Am Coll Cardiol 61(13):1421–1427. doi:10.1016/j.jacc.2012.09.065

7. Binu LS, Kumar AS (2012) Simulation of left main coronary bifurcation under different cases of stenosis and assessing the possibility of plaque proliferation using computational fluid dynamics. International Simulation Conference of India 2012

8. Binu LS, Kumar AS (2012) Simulation of left main coronary bifurcation lesions using 3D computational fluid dynamics model and its comparison with 2D. World Congress on Engineering 2012:631

9. Brown BG, Bolson EL, Dodge HT (1984) Dynamic mechanisms in human coronary stenosis. Circulation 70(6):917–922. doi:10.1161/01.CIR.70.6.917

10. Chaichana T, Sun Z, Jewkes J (2012) Investigation of the haemodynamic environment of bifurcation plaques within the left coronary artery in realistic patient models based on CT images. Australas Phys Eng Sci Med 35(2):231–236. doi:10.1007/s13246-012-0135-3

11. Chaichana T, Sun Z, Jewkes J (2013) Hemodynamic impacts of left coronary stenosis: a patient-specific analysis. Acta Bioeng Biomech 15(3):107–112. doi:10.5277/abb130313

12. Chaichana T, Sun Z, Jewkes J (2013) Haemodynamic analysis of the effect of different types of plaques in the left coronary artery. Comput Med Imaging Graph 37(3):197–206. doi:10.1016/j.compmedimag.2013.02.001

13. Chaichana T, Sun Z, Jewkes J (2011) Computation of hemodynamics in the left coronary artery with variable angulations. J Biomech 44(10):1869–1878. doi:10.1016/j.jbiomech.2011.04.033

14. Chaichana T, Sun Z, Jewkes J (2013) Hemodynamic impacts of various types of stenosis in the left coronary artery bifurcation: a patient-specific analysis. Phys Med 29(5):447–452. doi:10.1016/j.ejmp.2013.02.001

15. Chaichana T, Sun Z, Jewkes J (2012) Computational fluid dynamics analysis of the effect of plaques in the left coronary artery. Comput Math Methods Med 2012. doi:10.1155/2012/504367

16. Chaichana T, Sun Z, Jewkes J (2014) Impact of plaques in the left coronary artery on wall shear stress and pressure gradient in coronary side branches. Comput Methods Biomech Biomed Engin 17(2):108–118. doi:10.1080/10255842.2012.671308

17. Cho YI, Back LH, Crawford DW (1985) Effect of simulated hyperemia on the flow field in a mildly atherosclerotic coronary artery casting of man. Aviat Space Environ Med 56(3):212–219

18. Choi G, Cheng CP, Wilson NM, Taylor CA (2009) Methods for quantifying three-dimensional deformation of arteries due to

pulsatile and nonpulsatile forces: implications for the design of stents and stent grafts. Ann Biomed Eng 37(1):14–33. doi:10.1007/s10439-008-9590-0

19. Colombo A, Bramucci E, Sacca S, Violini R, Lettieri C, Zanini R, Sheiban I, Paloscia L, Grube E, Schofer J, Bolognese L, Orlandi M, Niccoli G, Latib A, Airoldi F (2009) Randomized study of the crush technique versus provisional side-branch stenting in true coronary bifurcations: the CACTUS (Coronary Bifurcations: Application of the Crushing Technique Using Sirolimus-Eluting Stents) Study. Circulation 119(1):71–78. doi:10.1161/CIRCULATIONAHA.108.808402

20. Daniels DV, van't Veer M, Pijls NH, van der Horst A, Yong AS, De Bruyne B, Fearon WF (2012) The impact of downstream coronary stenoses on fractional flow reserve assessment of intermediate left main disease. J Am Coll Cardiol: Cardiovasc Interv 5(10):1021–1025. doi:10.1016/j.jcin.2012.07.005

21. De Bruyne B, Bartunek J, Sys SU, Heyndrickx GR (1995) Relation between myocardial fractional flow reserve calculated from coronary pressure measurements and exercise-induced myocardial ischemia. Circulation 92(1):39–46. doi:10.1161/01.CIR.92.1.39

22. De Bruyne B, Bartunek J, Sys SU, Pijls NH, Heyndrickx GR, Wijns W (1996) Simultaneous coronary pressure and flow velocity measurements in humans. Feasibility, reproducibility, and hemodynamic dependence of coronary flow velocity reserve, hyperemic flow versus pressure slope index, and fractional flow reserve. Circulation 94(8):1842–1849. doi:10.1161/01.CIR.94.8.1842

23. Dodge JT Jr, Brown BG, Bolson EL, Dodge HT (1992) Lumen diameter of normal human coronary arteries. Influence of age, sex, anatomic variation, and left ventricular hypertrophy or dilation. Circulation 86(1):232–246. doi:10.1161/01.CIR.86.1.232

24. Esmaily Moghadam M, Vignon-Clementel IE, Figliola R, Marsden AL (2013) A modular numerical method for implicit 0D/3D coupling in cardiovascular finite element simulations. J Comput Phys 244(0):63–79. doi:10.1016/j.jcp.2012.07.035

25. Ferrari M, Werner GS, Bahrmann P, Richartz BM, Figulla HR (2006) Turbulent flow as a cause for underestimating coronary flow reserve measured by Doppler guide wire. Cardiovasc Ultrasound 4:14. doi:10.1186/1476-7120-4-14

26. Fischer JJ, Samady H, McPherson JA, Sarembock IJ, Powers ER, Gimple LW, Ragosta M (2002) Comparison between visual assessment and quantitative angiography versus fractional flow reserve for native coronary narrowings of moderate severity. Am J Cardiol 90(3):210–215. doi:10.1016/S0002-9149(02)02456-6

27. Frattolin J, Zarandi MM, Pagiatakis C, Bertrand OF, Mongrain R (2015) Numerical study of stenotic side branch hemodynamics in true bifurcation lesions. Comput Biol Med 57:130–138. doi:10.1016/j.compbiomed.2014.11.014

28. Gould K (1999) Coronary artery stenosis and reversing atherosclerosis. Arnold Publishers (Distributed in U.S. by Oxford University Press), London

29. Gould KL, Kirkeeide R, Johnson NP (2010) Coronary branch steal: experimental validation and clinical implications of interacting stenosis in branching coronary arteries. Circ Cardiovasc Imag 3(6):701–709. doi:10.1161/CIRCIMAGING.110.937656

30. Griffith MD, Leweke T, Thompson MC, Hourigan K (2013) Effect of small asymmetries on axisymmetric stenotic flow. J Fluid Mech 721:R1. doi:10.1017/jfm.2013.109

31. Hamilos M, Muller O, Cuisset T, Ntalianis A, Chlouverakis G, Sarno G, Nelis O, Bartunek J, Vanderheyden M, Wyffels E, Barbato E, Heyndrickx GR, Wijns W, De Bruyne B (2009) Long-term clinical outcome after fractional flow reserve-guided treatment in patients with angiographically equivocal left main coronary artery stenosis. Circulation 120(15):1505–1512. doi:10.1161/CIRCULATIONAHA.109.850073

32. Heywood JG, Rannacher R, Turek S (1996) Artificial boundaries and flux and pressure conditions for the incompressible Navier-Stokes equations. Int J Numer Meth Fl 22(5):325–352. doi:10.1002/(Sici)1097-0363(19960315)22:5<325::Aid-Fld307>3.0.Co;2-Y

33. Hsia TY, Cosentino D, Corsini C, Pennati G, Dubini G, Migliavacca F, Modeling of Congenital Hearts Alliance I (2011) Use of mathematical modeling to compare and predict hemodynamic effects between hybrid and surgical Norwood palliations for hypoplastic left heart syndrome. Circulation 124(11 Suppl):S204–S210. doi:10.1161/CIRCULATIONAHA.110.010769

34. Huo Y, Kassab GS (2012) Intraspecific scaling laws of vascular trees. J R Soc Interface 9(66):190–200. doi:10.1098/rsif.2011.0270

35. Huo Y, Kassab GS (2009) The scaling of blood flow resistance: from a single vessel to the entire distal tree. Biophys J 96(2):339–346. doi:10.1016/j.bpj.2008.09.038

36. Huo Y, Svendsen M, Choy JS, Zhang ZD, Kassab GS (2012) A validated predictive model of coronary fractional flow reserve. J R Soc Interface 9(71):1325–1338. doi:10.1098/rsif.2011.0605

37. Javadzadegan A, Shimizu Y, Behnia M, Ohta M (2013) Correlation between Reynolds number and eccentricity effect in stenosed artery models. Technol Health Care 21(4):357–367. doi:10.3233/THC-130736

38. Javadzadegan A, Yong AS, Chang M, Ng AC, Yiannikas J, Ng MK, Behnia M, Kritharides L (2013) Flow recirculation zone length and shear rate are differentially affected by stenosis severity in human coronary arteries. Am J Physiol Heart Circ Physiol 304(4):H559–H566. doi:10.1152/ajpheart.00428.2012

39. Jeon BJ, Kim J, Choi HG (2015) A finite element analysis of turbulent eccentric stenotic flows by large eddy simulation. J Mech Sci Technol 29(5):1869–1874. doi:10.1007/s12206-015-0407-4

40. Kelle S, Hays AG, Hirsch GA, Gerstenblith G, Miller JM, Steinberg AM, Schar M, Texter JH, Wellnhofer E, Weiss RG, Stuber M (2011) Coronary artery distensibility assessed by 3.0 Tesla coronary magnetic resonance imaging in subjects with and without coronary artery disease. Am J Cardiol 108(4):491–497. doi:10.1016/j.amjcard.2011.03.078

41. Kim HJ, Vignon-Clementel IE, Coogan JS, Figueroa CA, Jansen KE, Taylor CA (2010) Patient-specific modeling of blood flow and pressure in human coronary arteries. Ann Biomed Eng 38(10):3195–3209. doi:10.1007/s10439-010-0083-6

42. Koo BK, Waseda K, Kang HJ, Kim HS, Nam CW, Hur SH, Kim JS, Choi D, Jang Y, Hahn JY, Gwon HC, Yoon MH, Tahk SJ, Chung WY, Cho YS, Choi DJ, Hasegawa T, Kataoka T, Oh SJ, Honda Y, Fitzgerald PJ, Fearon WF (2010) Anatomic and functional evaluation of bifurcation lesions undergoing percutaneous coronary intervention. Circ Cardiovasc Interv 3(2):113–119. doi:10.1161/CIRCINTERVENTIONS.109.887406

43. Koo BK, Park KW, Kang HJ, Cho YS, Chung WY, Youn TJ, Chae IH, Choi DJ, Tahk SJ, Oh BH, Park YB, Kim HS (2008) Physiological evaluation of the provisional side-branch intervention strategy for bifurcation lesions using fractional flow reserve. Eur Heart J 29(6):726–732. doi:10.1093/eurheartj/ehn045

44. Lagana K, Balossino R, Migliavacca F, Pennati G, Bove EL, de Leval MR, Dubini G (2005) Multiscale modeling of the cardiovascular system: application to the study of pulmonary and coronary perfusions in the univentricular circulation. J Biomech 38(5):1129–1141. doi:10.1016/j.jbiomech.2004.05.027

45. Latib A, Colombo A (2008) Bifurcation disease: what do we know, what should we do? J Am Coll Cardiol: Cardiovasc Interv 1(3):218–226. doi:10.1016/j.jcin.2007.12.008

46. Levy MN, Pappano AJ, Berne RM (2007) The cardiac pump. Cardiovascular physiology. Mosby Elsevier, Philadelphia, p 74

47. Li J, Elrashidi MY, Flammer AJ, Lennon RJ, Bell MR, Holmes DR, Bresnahan JF, Rihal CS, Lerman LO, Lerman A (2013) Long-term outcomes of fractional flow reserve-guided vs. angiography-guided percutaneous coronary intervention in contemporary practice. Eur Heart J 34(18):1375–1383. doi:10.1093/eurheartj/eht005

48. Louvard Y, Thomas M, Dzavik V, Hildick-Smith D, Galassi AR, Pan M, Burzotta F, Zelizko M, Dudek D, Ludman P, Sheiban I, Lassen JF, Darremont O, Kastrati A, Ludwig J, Iakovou I, Brunel P, Lansky A, Meerkin D, Legrand V, Medina A, Lefevre T (2008) Classification of coronary artery bifurcation lesions and treatments: time for a consensus! Catheter Cardiovasc Interv 71(2): 175–183. doi:10.1002/ccd.21314

49. Maehara A, Mintz GS, Castagna MT, Pichard AD, Satler LF, Waksman R, Laird JR Jr, Suddath WO, Kent KM, Weissman NJ (2001) Intravascular ultrasound assessment of the stenoses location and morphology in the left main coronary artery in relation to anatomic left main length. Am J Cardiol 88(1):1–4. doi:10.1016/S0002-9149(01)01575-2

50. Mallinger F, Drikakis D (2002) Instability in three-dimensional, unsteady, stenotic flows. Int J Heat Fluid Fl 23(5):657–663. doi:10.1016/S0142-727x(02)00161-3

51. Mantero S, Pietrabissa R, Fumero R (1992) The coronary bed and its role in the cardiovascular system: a review and an introductory single-branch model. J Biomed Eng 14(2):109–116. doi:10.1016/0141-5425(92)90015-D

52. Medina A, Suarez de Lezo J, Pan M (2006) A new classification of coronary bifurcation lesions. Rev Esp Cardiol 59(2):183. doi:10.1016/S1885-5857(06)60130-8

53. Medina A, Martin P, Suarez de Lezo J, Novoa J, Melian F, Hernandez E, Suarez de Lezo J, Pan M, Burgos L, Amador C, Morera O, Garcia A (2011) Ultrasound study of the prevalence of plaque at the carina in lesions that affect the coronary bifurcation. Implications for treatment with provisional stent. Rev Esp Cardiol 64(1):43–50. doi:10.1016/j.recesp.2010.07.006

54. Meimoun P, Sayah S, Luycx-Bore A, Boulanger J, Elmkies F, Benali T, Zemir H, Doutrelan L, Clerc J (2011) Comparison between non-invasive coronary flow reserve and fractional flow reserve to assess the functional significance of left anterior descending artery stenosis of intermediate severity. J Am Soc Echocardiogr 24(4):374–381. doi:10.1016/j.echo.2010.12.007

55. Melih Guleren K (2013) Numerical flow analysis of coronary arteries through concentric and eccentric stenosed geometries. J Biomech 46(6):1043–1052. doi:10.1016/j.jbiomech.2013.02.001

56. Migliavacca F, Balossino R, Pennati G, Dubini G, Hsia TY, de Leval MR, Bove EL (2006) Multiscale modelling in biofluidynamics: application to reconstructive paediatric cardiac surgery. J Biomech 39(6):1010–1020. doi:10.1016/j.jbiomech.2005.02.021

57. Mittal R, Simmons SP, Najjar F (2003) Numerical study of pulsatile flow in a constricted channel. J Fluid Mech 485:337–378. doi:10.1017/S002211200300449x

58. Morris PD, van de Vosse FN, Lawford PV, Hose DR, Gunn JP (2015) "Virtual" (computed) fractional flow reserve: current challenges and limitations. J Am Coll Cardiol: Cardiovasc Interv 8(8):1009–1017. doi:10.1016/j.jcin.2015.04.006

59. Morris PD, Ryan D, Morton AC, Lycett R, Lawford PV, Hose DR, Gunn JP (2013) Virtual fractional flow reserve from coronary angiography: modeling the significance of coronary lesions: results from the VIRTU-1 (VIRTUal Fractional Flow Reserve From Coronary Angiography) study. J Am Coll Cardiol: Cardiovasc Interv 6(2):149–157. doi:10.1016/j.jcin.2012.08.024

60. Natsumeda M, Nakazawa G, Murakami T, Torii S, Ijichi T, Ohno Y, Masuda N, Shinozaki N, Ogata N, Yoshimachi F (2015) Coronary angiographic characteristics that influence fractional flow reserve. Circ J. doi:10.1253/circj.CJ-14-0931

61. Norgaard BL, Leipsic J, Gaur S, Seneviratne S, Ko BS, Ito H, Jensen JM, Mauri L, De Bruyne B, Bezerra H, Osawa K, Marwan M, Naber C, Erglis A, Park SJ, Christiansen EH, Kaltoft A, Lassen JF, Botker HE, Achenbach S, Group NXTTS (2014) Diagnostic performance of noninvasive fractional flow reserve derived from coronary computed tomography angiography in suspected coronary artery disease: the NXT trial (Analysis of Coronary Blood Flow Using CT Angiography: Next Steps). J Am Coll Cardiol 63(12):1145–1155. doi:10.1016/j.jacc.2013.11.043

62. Opolski MP, Kepka C, Achenbach S, Pregowski J, Kruk M, Staruch AD, Kadziela J, Ruzyllo W, Witkowski A (2013) Advanced computed tomographic anatomical and morphometric plaque analysis for prediction of fractional flow reserve in intermediate coronary lesions. Eur J Radiol 83(1):135–141. doi:10.1016/j.ejrad.2013.10.005

63. Oviedo C, Maehara A, Mintz GS, Araki H, Choi SY, Tsujita K, Kubo T, Doi H, Templin B, Lansky AJ, Dangas G, Leon MB, Mehran R, Tahk SJ, Stone GW, Ochiai M, Moses JW (2010) Intravascular ultrasound classification of plaque distribution in left main coronary artery bifurcations: where is the plaque really located? Circ Cardiovasc Interv 3(2):105–112. doi:10.1161/Circinterventions.109.906016

64. Pagiatakis C, Tardif JC, L'Allier PL, Mongrain R (2015) A numerical investigation of the functionality of coronary bifurcation lesions with respect to lesion configuration and stenosis severity. J Biomech 48(12):3103–3111. doi:10.1016/j.jbiomech.2015.07.018

65. Papadopoulou SL, Girasis C, Gijsen FJ, Rossi A, Ottema J, van der Giessen AG, Schuurbiers JC, Garcia-Garcia HM, de Feyter PJ, Wentzel JJ (2014) A CT-based Medina classification in coronary bifurcations: does the lumen assessment provide sufficient information? Catheter Cardiovasc Interv 84(3):445–452. doi:10.1002/ccd.25496

66. Pietrabissa R, Mantero S, Marotta T, Menicanti L (1996) A lumped parameter model to evaluate the fluid dynamics of different coronary bypasses. Med Eng Phys 18(6):477–484. doi:10.1016/1350-4533(96)00002-1

67. Pijls NH, Sels JW (2012) Functional measurement of coronary stenosis. J Am Coll Cardiol 59(12):1045–1057. doi:10.1016/j.jacc.2011.09.077

68. Pijls NH, van Son JA, Kirkeeide RL, De Bruyne B, Gould KL (1993) Experimental basis of determining maximum coronary, myocardial, and collateral blood flow by pressure measurements for assessing functional stenosis severity before and after percutaneous transluminal coronary angioplasty. Circulation 87(4):1354–1367. doi:10.1161/01.CIR.87.4.1354

69. Pijls NH (2013) Fractional flow reserve to guide coronary revascularization. Circ J 77(3):561–569. doi:10.1253/circj.CJ-13-0161

70. Pijls NH, De Bruyne B, Bech GJ, Liistro F, Heyndrickx GR, Bonnier HJ, Koolen JJ (2000) Coronary pressure measurement to assess the hemodynamic significance of serial stenoses within one coronary artery: validation in humans. Circulation 102(19):2371–2377. doi:10.1161/01.CIR.102.19.2371

71. Pijls NHJ, Vangelder B, Vandervoort P, Peels K, Bracke FALE, Bonnier HJRM, Elgamal MIH (1995) Fractional flow reserve—a useful index to evaluate the influence of an epicardial coronary stenosis on myocardial blood-flow. Circulation 92(11):3183–3193. doi:10.1161/01.CIR.92.11.3183

72. Poepping TL, Rankin RN, Holdsworth DW (2010) Flow patterns in carotid bifurcation models using pulsed Doppler ultrasound: effect of concentric vs. eccentric stenosis on turbulence and recirculation. Ultrasound Med Biol 36(7):1125–1134. doi:10.1016/j.ultrasmedbio.2010.02.005

73. Prosi M, Perktold K, Ding Z, Friedman MH (2004) Influence of curvature dynamics on pulsatile coronary artery flow in a realistic

bifurcation model. J Biomech 37(11):1767–1775. doi:10.1016/j.jbiomech.2004.01.021

74. Quarteroni A, Ragni S, Veneziani A (2001) Coupling between lumped and distributed models for blood flow problems. Comput Vis Sci 4(2):111–124. doi:10.1007/s007910100063

75. Quarteroni A, Veneziani A (2003) Analysis of a geometrical multiscale model based on the coupling of ODEs and PDEs for blood flow simulations. Multiscale Model Sim 1(2):173–195. doi:10.1137/S1540345902408482

76. Ragosta M (2015) Left main coronary artery disease: importance, diagnosis, assessment, and management. Curr Probl Cardiol 40(3):93–126. doi:10.1016/j.cpcardiol.2014.11.003

77. Rodriguez-Granillo GA, Rosales MA, Degrossi E, Durbano I, Rodriguez AE (2007) Multislice CT coronary angiography for the detection of burden, morphology and distribution of atherosclerotic plaques in the left main bifurcation. Int J Cardiovasc Imaging 23(3):389–392. doi:10.1007/s10554-006-9144-1

78. Rubinshtein R, Lerman A, Spoon DB, Rihal CS (2012) Anatomic features of the left main coronary artery and factors associated with its bifurcation angle: a 3-dimensional quantitative coronary angiographic study. Catheter Cardiovasc Interv 80(2):304–309. doi:10.1002/ccd.23425

79. Sankaran S, Esmaily Moghadam M, Kahn AM, Tseng EE, Guccione JM, Marsden AL (2012) Patient-specific multiscale modeling of blood flow for coronary artery bypass graft surgery. Ann Biomed Eng 40(10):2228–2242. doi:10.1007/s10439-012-0579-3

80. Scanlon PJ, Faxon DP, Audet AM, Carabello B, Dehmer GJ, Eagle KA, Legako RD, Leon DF, Murray JA, Nissen SE, Pepine CJ, Watson RM, Ritchie JL, Gibbons RJ, Cheitlin MD, Gardner TJ, Garson A Jr, Russell RO Jr, Ryan TJ, Smith SC Jr (1999) ACC/AHA guidelines for coronary angiography. A report of the American College of Cardiology/American Heart Association Task Force on practice guidelines (Committee on Coronary Angiography). Developed in collaboration with the Society for Cardiac Angiography and Interventions. J Am Coll Cardiol 33(6):1756–1824. doi:10.1161/01.CIR.99.17.2345

81. Segers P, Stergiopulos N, Westerhof N, Wouters P, Kolh P, Verdonck P (2003) Systemic and pulmonary hemodynamics assessed with a lumped-parameter heart-arterial interaction model. J Eng Math 47(3–4):185–199. doi:10.1023/B:Engi.0000007975.27377.9c

82. Seiler C (2010) The human coronary collateral circulation. Eur J Clin Investig 40(5):465–476. doi:10.1111/j.1365-2362.2010.02282.x

83. Sen S, Escaned J, Malik IS, Mikhail GW, Foale RA, Mila R, Tarkin J, Petraco R, Broyd C, Jabbour R, Sethi A, Baker CS, Bellamy M, Al-Bustami M, Hackett D, Khan M, Lefroy D, Parker KH, Hughes AD, Francis DP, Di Mario C, Mayet J, Davies JE (2012) Development and validation of a new adenosine-independent index of stenosis severity from coronary wave-intensity analysis: results of the ADVISE (ADenosine Vasodilator Independent Stenosis Evaluation) study. J Am Coll Cardiol 59(15):1392–1402. doi:10.1016/j.jacc.2011.11.003

84. Senzaki H, Chen CH, Kass DA (1996) Single-beat estimation of end-systolic pressure-volume relation in humans. A new method with the potential for noninvasive application. Circulation 94(10):2497–2506. doi:10.1161/01.CIR.94.10.2497

85. Shaw JA, Kingwell BA, Walton AS, Cameron JD, Pillay P, Gatzka CD, Dart AM (2002) Determinants of coronary artery compliance in subjects with and without angiographic coronary artery disease. J Am Coll Cardiol 39(10):1637–1643. doi:10.1016/S0735-1097(02)01842-9

86. Sherwin SJ, Blackburn HM (2005) Three-dimensional instabilities and transition of steady and pulsatile axisymmetric stenotic flows. J Fluid Mech 533:297–327. doi:10.1017/S0022112005004271

87. Takagi A, Tsurumi Y, Ishii Y, Suzuki K, Kawana M, Kasanuki H (1999) Clinical potential of intravascular ultrasound for physiological assessment of coronary stenosis: relationship between quantitative ultrasound tomography and pressure-derived fractional flow reserve. Circulation 100(3):250–255. doi:10.1161/01.CIR.100.3.250

88. Takashima H, Waseda K, Gosho M, Kurita A, Ando H, Sakurai S, Maeda K, Kumagai S, Suzuki A, Amano T (2015) Severity of morphological lesion complexity affects fractional flow reserve in intermediate coronary stenosis. J Cardiol 66(3):239–245. doi:10.1016/j.jjcc.2014.11.004

89. Toggweiler S, Urbanek N, Schoenenberger AW, Erne P (2010) Analysis of coronary bifurcations by intravascular ultrasound and virtual histology. Atherosclerosis 212(2):524–527. doi:10.1016/j.atherosclerosis.2010.06.045

90. Tonino PA, Fearon WF, De Bruyne B, Oldroyd KG, Leesar MA, Ver Lee PN, Maccarthy PA, Van't Veer M, Pijls NH (2010) Angiographic versus functional severity of coronary artery stenoses in the FAME study fractional flow reserve versus angiography in multivessel evaluation. J Am Coll Cardiol 55(25):2816–2821. doi:10.1016/j.jacc.2009.11.096

91. Turgut O, Yilmaz A, Yalta K, Yilmaz BM, Ozyol A, Kendirlioglu O, Karadas F, Tandogan I (2007) Tortuosity of coronary arteries: an indicator for impaired left ventricular relaxation? Int J Cardiovasc Imaging 23(6):671–677. doi:10.1007/s10554-006-9186-4

92. Varghese SS, Frankel SH, Fischer PF (2007) Direct numerical simulation of stenotic flows. Part 2. Pulsatile flow. J Fluid Mech 582:281–318. doi:10.1017/S0022112007005836

93. Varghese SS, Frankel SH, Fischer PF (2008) Modeling transition to turbulence in eccentric stenotic flows. J Biomech Eng 130(1):014503. doi:10.1115/1.2800832

94. Vignon-Clementel IE, Alberto Figueroa C, Jansen KE, Taylor CA (2006) Outflow boundary conditions for three-dimensional finite element modeling of blood flow and pressure in arteries. Comput Method Appl Mech Eng 195(29–32):3776–3796. doi:10.1016/j.cma.2005.04.014

95. Wang JZ, Tie B, Welkowitz W, Kostis J, Semmlow J (1989) Incremental network analogue model of the coronary artery. Med Biol Eng Comput 27(4):416–422. doi:10.1007/BF02441434

96. White CW, Wright CB, Doty DB, Hiratza LF, Eastham CL, Harrison DG, Marcus ML (1984) Does visual interpretation of the coronary arteriogram predict the physiologic importance of a coronary stenosis? N Engl J Med 310(13):819–824. doi:10.1056/NEJM198403293101304

97. Williams MJ, Stewart RA, Low CJ, Wilkins GT (1999) Assessment of the mechanical properties of coronary arteries using intravascular ultrasound: an in vivo study. Int J Card Imaging 15(4):287–294. doi:10.1023/A:1006279228534

98. Windecker S, Kolh P, Alfonso F, Collet JP, Cremer J, Falk V, Filippatos G, Hamm C, Head SJ, Juni P, Kappetein AP, Kastrati A, Knuuti J, Landmesser U, Laufer G, Neumann FJ, Richter DJ, Schauerte P, Sousa Uva M, Stefanini GG, Taggart DP, Torracca L, Valgimigli M, Wijns W, Witkowski A (2014) 2014 ESC/EACTS guidelines on myocardial revascularization: the Task Force on Myocardial Revascularization of the European Society of Cardiology (ESC) and the European Association for Cardio-Thoracic Surgery (EACTS) developed with the special contribution of the European Association of Percutaneous Cardiovascular Interventions (EAPCI). Eur Heart J 35(37):2541–2619. doi:10.1093/eurheartj/ehu278

99. Yong AS, Daniels D, De Bruyne B, Kim HS, Ikeno F, Lyons J, Pijls NH, Fearon WF (2013) Fractional flow reserve assessment of left main stenosis in the presence of downstream coronary stenoses. Circ Cardiovasc Interv 6(2):161–165. doi:10.1161/CIRCINTERVENTIONS.112.000104

100. Yong AS, Ng AC, Brieger D, Lowe HC, Ng MK, Kritharides L (2011) Three-dimensional and two-dimensional quantitative coronary angiography, and their prediction of reduced fractional flow reserve. Eur Heart J 32(3):345–353. doi:10.1093/eurheartj/ehq259

101. Young DF, Tsai FY (1973) Flow characteristics in models of arterial stenoses—I. Steady flow. J Biomech 6(4):395–410. doi:10.1016/0021-9290(73)90099-7

102. Young DF, Tsai FY (1973) Flow characteristics in models of arterial stenoses. II. Unsteady flow. J Biomech 6(5):547–559. doi:10.1016/0021-9290(73)90012-2

103. Zarandi M, Mongrain R, Bertrand O (2012) Determination of flow conditions in coronary bifurcation lesions in the context of the Medina classification. Model Simulat Eng; 2012(2012), DOI:10.1155/2012/419087

104. Zhang JM, Zhong L, Luo T, Huo Y, Tan SY, Wong AS, Su B, Wan M, Zhao X, Kassab GS, Lee HP, Khoo BC, Kang CW, Ba T, Tan RS (2014) Numerical simulation and clinical implications of stenosis in coronary blood flow. Biomed Res Int 2014:514729. doi:10.1155/2014/514729

105. Zhu H, Ding Z, Piana RN, Gehrig TR, Friedman MH (2009) Cataloguing the geometry of the human coronary arteries: a potential tool for predicting risk of coronary artery disease. Int J Cardiol 135(1):43–52. doi:10.1016/j.ijcard.2008.03.087

Catherine Pagiatakis obtained her doctorate degree from the Department of Mechanical Engineering at McGill University.

Jean-Claude Tardif is the director of the Montreal Heart Institute Research Centre and a professor of medicine at Université de Montréal.

Philippe L. L'Allier is an associate professor at Université de Montréal and the director of the Hemodynamics/Interventional Cardiology Laboratory at the Montreal Heart Institute.

Rosaire Mongrain is an associate professor of Mechanical Engineering at McGill University.